PERFORMANCE OF A SIX DEGREE-OF-FREEDOM PRECISION POINTING TEST RIG USING SLOTLESS SELF-BEARING MOTORS

Zhaohui Ren, Lyndon Scott Stephens
University of Kentucky, Bearings and Seals Laboratory
Department of Mechanical Engineering, 151 RGAN, Lexington, KY 40506
zren0@engr.uky.edu, stephens@engr.uky.edu

ABSTRACT

The slotless self-bearing motor (SBM) technology is first utilized to fully provide bearing and motoring functionality simultaneously in a six degree-of-freedom (DOF) prototype gimbal system, to demonstrate its precision pointing and smooth angular slewing capability. The novel six DOF magnetic actuator incorporates two SBMs to produce both radial bearing forces and motoring torque and one conventional thrust active magnetic bearing (AMB) to provide axial support. The dynamic model of the system is developed and a set of six decoupled PID controllers is designed based on the theoretical model. The closed loop performance of the system confirms experimentally that these controllers provide stable levitation and smooth angular slewing. The most encouraging result is that the actuator is capable of pointing down to less than 377 nrad angularly.

INTRODUCTION

Gimbals in space-based precision pointing systems currently employ mechanical bearings. Mechanical bearings' inherent reliability and functionality debits ultimately limit gimbal life and functional sophistication. Advances in electromagnetic suspension and electronic drive technology point the way for new gimbals with great potential for significant improvement on pointing accuracy, reliability, weight and power consumption efficiency, maintainability and gimbal life among other features, additionally they can provide active vibration isolation to sensitive payloads due to their active control ability.

A new permanent magnet (PM) SBM design [1-5] generates both radial bearing forces and motoring torque using common coils and return flux path, eliminates the trade-off between torque and bearing force production and the stator teeth that can saturate and limit peak torque shown in other designs [6,7]. The slotless stator construction allows for a smoother torque generation, making it advantageous for precision pointing and smooth angular slewing applications. To demonstrate the precision pointing gimbal with higher power density beneficial from the new design, a prototype gimbal system is designed and constructed. This novel six DOF magnetic actuator incorporates two such slotless SBMs and one conventional thrust AMB, thus allows for a complete electromagnetic suspension and precision pointing.

Some work has been done on a test rig which incorporates one slotless SBM to produce the motoring torque and replace a conventional AMB to support one end of the shaft radially. [3] derived the linearized force-current-displacement relationship for the SBM, [8] discussed a detailed dynamic model for the test rig, [9,10] presented the closed-loop performance of the test rig. Previous work has shown that the slotless SBM and its associated control are able to point down to the resolution of the feedback devices. In this paper, the linear model for the gimbal system is described that is used to design a set of six decoupled PID controllers. The actuator is successfully levitated in all DOF using these controllers. Tracking performance of the closed loop system is investigated and confirms that these controllers provide stable levitation and smooth angular slewing. The pointing accuracy of the actuator is determined to be less than 377 nrad angularly.

TEST RIG DESCRIPTION

Figure 1 is an overview of the prototype gimbal test rig, its systematic diagram is shown in Fig. 2. The test rig consists of two slotless SBMs with a thrust AMB in between, one cylindrical sensor plate attached to each end of the rotor. A linear reflective metal tape is wrapped around the outer diameter of each plate and being targeted by four encoder read heads. Each SBM has PM poles attached circumferentially to the outer diameter of the cylindrical rotor and windings attached to the inner diameter of the slotless stator back iron.

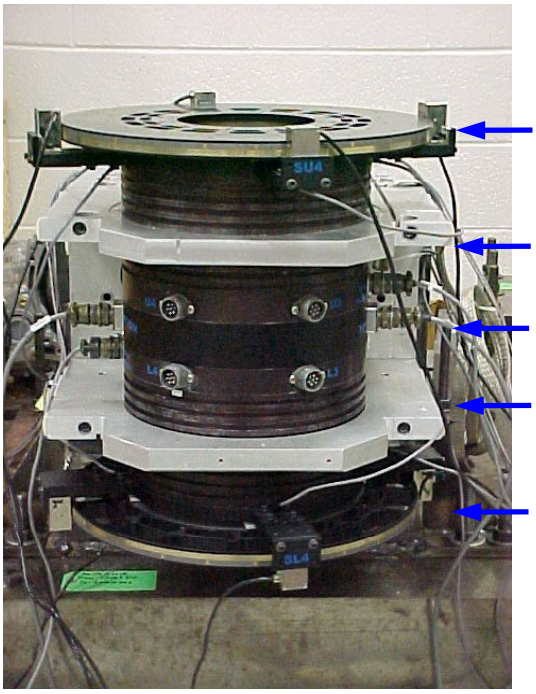

Figure 1. Test rig on the test stand

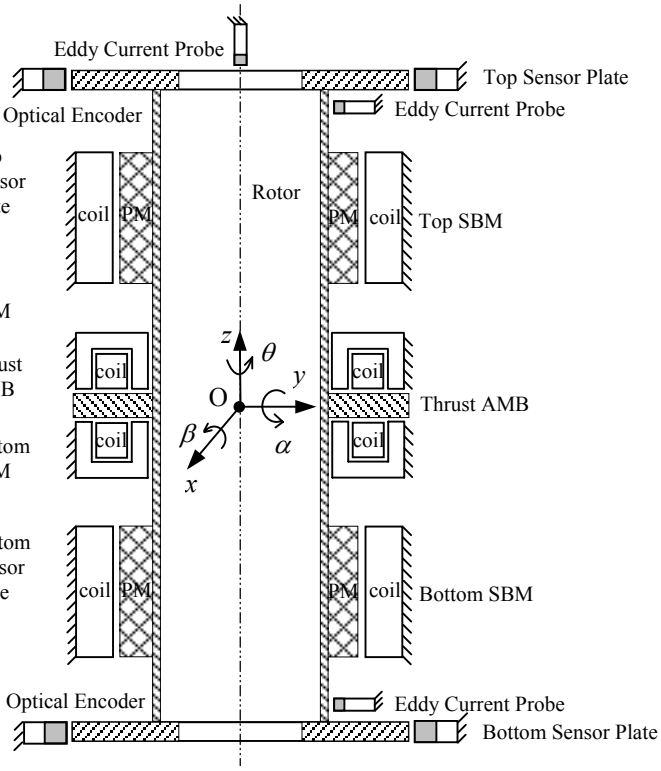

Figure 2. Test rig systematic

The thrust AMB utilized at the mid-span of the rotor is a typical cylindrical type AMB with a separate stator winding on each side of a rotor mounted thrust disk.

Currently, the eight incremental encoders 90° apart provide the angular displacement measurement with ultra-high resolution, two eddy current probes 90° apart from each other are installed next to each sensor plate as feedback devices for the radial displacements at each end of the shaft, and a single eddy current probe is positioned close to the center of the top sensor plate to measure the shaft axial displacement for feedback control purpose, as illustrated in Fig. 2.

DYNAMIC SYSTEM MODEL

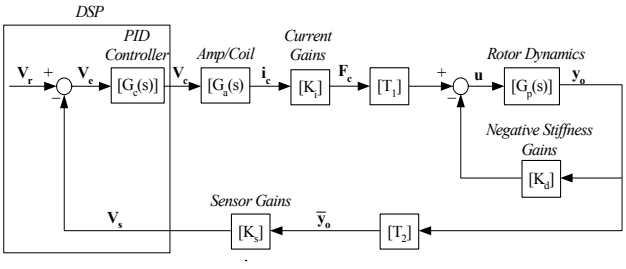

Figure 3. Linear system model for controller design

An analytical model of the system is developed for controller design, including detailed models for the shaft rotor dynamics, SBM and thrust AMB actuators, power amplifiers, angular and linear position sensors. The linearized actuator model is characterized by the current and negative stiffness gains for both SBMs and thrust AMB. Figure 3 shows the block diagram of the linear system model, with each component discussed in the following sections.

Shaft Rotor Dynamics

As shown in Fig. 2, the shaft assembly consists of the sensor plate for the top motor bearing, the top SBM rotor with PMs attached, a rotor mounted thrust disk for the thrust bearing, the bottom SBM rotor with PMs attached, and the sensor plate for the bottom motor bearing.

The lateral rotor dynamic model includes five free-free rigid body modes: one bouncing mode in each of the *x, y* and *z* directions, one tilting mode in each of the *x-z* and *y-z* planes. Because of the precision pointing requirement, the torsional rotor dynamic model is generated using 4 lumped mass stations at top sensor plate, top SBM actuator, bottom SBM actuator and bottom sensor plate respectively, connected by mass less torsional springs. The overall governing dynamic equations have the following 2nd order form:

$$\begin{bmatrix} m & & & & & \\ & m & & & & \\ & & m & & & \\ & & & I_T & & \\ & & & & I_T & \\ & & & & & [I_p] \end{bmatrix} \begin{Bmatrix} \ddot{x} \\ \ddot{y} \\ \ddot{z} \\ \ddot{\alpha} \\ \ddot{\beta} \\ \ddot{\boldsymbol{\theta}} \end{Bmatrix} + \begin{bmatrix} 0 & & & & & \\ & 0 & & & & \\ & & 0 & & & \\ & & & 0 & & \\ & & & & 0 & \\ & & & & & [K_\theta] \end{bmatrix} \begin{Bmatrix} x \\ y \\ z \\ \alpha \\ \beta \\ \boldsymbol{\theta} \end{Bmatrix}$$

$$= \begin{bmatrix} \mathbf{C_x} & 0 & 0 & 0 \\ 0 & \mathbf{C_y} & 0 & 0 \\ 0 & 0 & 1 & 0 \\ \mathbf{C_\alpha} & 0 & 0 & 0 \\ 0 & \mathbf{C_\beta} & 0 & 0 \\ 0 & 0 & 0 & [I_4] \end{bmatrix} \begin{Bmatrix} \mathbf{F_x} \\ \mathbf{F_y} \\ F_z \\ \mathbf{T_\theta} \end{Bmatrix} \quad (1)$$

where m is the total mass, I_T is the transverse mass moments of inertia, x, y and z are the lateral bouncing displacements, α and β are the angular tilting displacements, $\mathbf{F_x}$ and $\mathbf{F_y}$ are the force vectors in x and y directions at locations such as top radial probes, top SBM actuator, bottom SBM actuator and bottom radial probes, F_z is the force in z direction, $[I_p]$ and $[K_\theta]$ are polar mass moments of inertia and stiffness matrices, $\boldsymbol{\theta}$ and $\mathbf{T_\theta}$ are angular displacement and torque vectors at locations of top sensor plate, top SBM actuator, bottom SBM actuator and bottom sensor plate, $\mathbf{C_x}$, $\mathbf{C_y}$, $\mathbf{C_\alpha}$ and $\mathbf{C_\beta}$ are coefficient vectors.

The 2nd order Eq. (1) is readily converted to the following state-space form:

$$\dot{\mathbf{w}} = [A]\mathbf{w} + [B]\mathbf{u}$$
$$\mathbf{y_o} = [C]\mathbf{w} \quad (2)$$

where $\mathbf{w}$ is the state vector, $\mathbf{u}$ is the vector of force and torque inputs and $\mathbf{y_o}$ is the vector of displacement outputs. The rotor dynamics transfer function matrix $[G_p(s)]$ relating $\mathbf{y_o}$ to $\mathbf{u}$ in Fig. 3 is then computed as:

$$[G_p(s)] = [C][sI - A]^{-1}[B] \quad (3)$$

SBM Actuator

Figure 4 shows the layout of one slotless SBM consisting of M=12 PM pole pairs attached to the rotor and N_{seg}=4 individually controlled motor bearing winding segments attached to a slotless stator back iron. The windings occupy N_s=18 stations along each segment ID of $\pi/2$ radians with N_w=96 individual wires per station. The 18 stations are divided into 6 sets of 3 phase windings. Table 1 summarizes the properties of the SBM.

Figure 4 also illustrates how the 4 segment currents i_1 - i_4 are related to the 3 directional control currents i_x, i_y and i_θ [3]. Therefore, the four segment forces F_{1x}, F_{2y}, F_{3x} and F_{4y} due to the PM flux linking with the segment windings are resolved into the independent net bearing forces F_x, F_y and motoring torque T_θ.

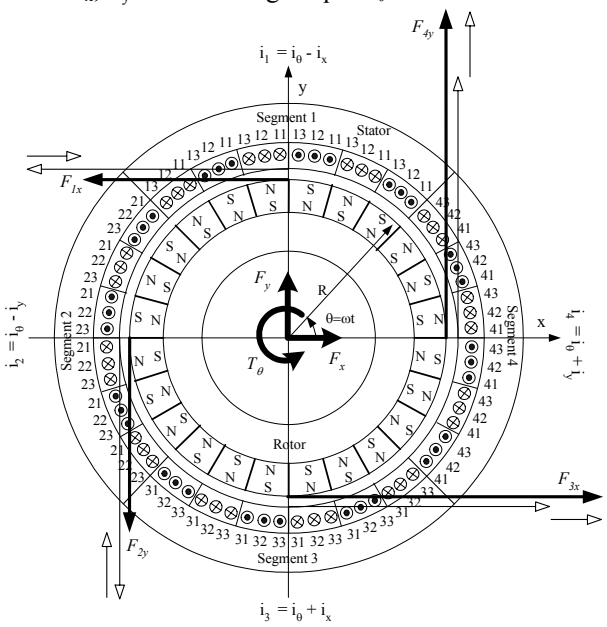

Figure 4. Slotless SBM layout

Table 1. SBM and thrust AMB property summary

	Property	Symbol	Value	Unit
SBM	No. of pole pairs	M	12	--
	No. of segments	N_{seg}	4	--
	No. of phases / segment	N_φ	3	--
	No. of winding stations / segment	N_s	18	--
	No. of wires / winding station	N_w	96	--
	Radial thickness of PMs	t_m	10.16	*mm*
	Radial thickness of coil windings	t_c	4.826	*mm*
	Nominal radial air gap	$g_{o,m}$	0.635	*mm*
	Rotor outer radius	R	110.05	*mm*
	Motor length	L	101.6	*mm*
	PM width	W_m	25.4	*mm*
	Width of one pole pitch	W_p	28.81	*mm*
	Recoil permeability	μ_R	1.05	--
	Remnance flux density	B_r	1.35	*T*
AMB	No. of phases	N_p	2	--
	No. of wires / phase	N	135	--
	Bias current	I_b	4.0	*A*
	Nominal axial air gap	$g_{o,z}$	0.508	*mm*

The linearized force-current-displacement relation for the slotless SBM is characterized by a current gain matrix $[K_{i,m}]$ and a negative stiffness (destabilizing) matrix $[K_{d,m}]$. The results from [3] are used directly for the two SBMs in this system, please refer to the original paper for the details.

Thrust AMB Actuator

The thrust AMB is a typical cylindrical Maxwell type AMB, consisting of a thrust disk mounted on the rotor mid-span and a separate winding inside the stator back iron at either side of the disk. The schematic of

thrust AMB is shown in Fig. 5, where N is the number of wires per thrust coil, A_p is the pole area, m is the total mass of the shaft assembly.

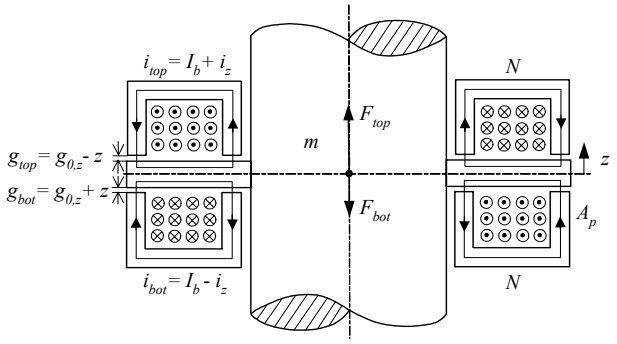

Figure 5. Thrust AMB schematic

As depicted in Fig. 5, the currents in the top and bottom thrust coils i_{top} and i_{bot} can be split into a constant bias current I_b and a varying perturbation current i_z, the instantaneous air gaps g_{top} and g_{bot} can be written in terms of the nominal axial air gap $g_{0,z}$ occurring when the thrust disk is centered and the displacement of the disk from the centered position z, the net force generated by the thrust AMB to provide stable levitation in the vertical z direction is given by:

$$F_z = F_{top} - F_{bot} = \frac{\mu_0 A_p N^2}{4}\left(\frac{(I_b + i_z)^2}{(g_{0,z} - z)^2} - \frac{(I_b - i_z)^2}{(g_{0,z} + z)^2}\right) = K_{i,z} i_z + K_{d,z} z \tag{4}$$

where the non-linear force has been linearized with respect to the perturbation current i_z and the displacement z, $K_{i,z}$ and $K_{d,z}$ are the current and the destabilizing negative stiffness gains for the thrust actuator. The properties of the thrust AMB are also included in Table 1.

The current gain matrix $[K_i]$ in Fig. 3 combines $[K_{i,m}]$ and $K_{i,z}$ based on the control current and force vectors $\mathbf{i_c}$ and $\mathbf{F_c}$, similarly the negative stiffness gain matrix $[K_d]$ combines $[K_{d,m}]$and $K_{d,z}$ based on the force input and displacement output vectors $\mathbf{u}$ and $\mathbf{y_o}$. $[T_1]$ simply distributes $\mathbf{F_c}$ into $\mathbf{u}$.

Sensors

The angular position sensors are optical encoders, the radial and axial position sensors are inductive type probes. They are modeled as pure gains on the diagonal of the sensor gain matrix $[K_s]$, relating the displacement of interest vector $\overline{\mathbf{y_o}}$ selected from $\mathbf{y_o}$ by $[T_2]$ to the sensor measurement vector $\mathbf{V_s}$, as shown in Fig. 3.

The sensitivity of each probe combines the linear calibration curves, measured using the probe and target, and the scaling factors inside the DSP. Each encoder has an angular resolution of 4.9μrad, and the eight encoder readings are averaged to get the angular measurement, the theoretical resolution of the encoder system is 153nrad after averaging and quadrature.

Power Amplifiers

The power amplifiers are PWM transconductance amplifiers that drive the 12 phase coils of each SBM and the 2 phase coils of the thrust AMB. Therefore, there are totally 26 amplifiers working in the single-phase mode. The transfer function of each amp/coil pair is measured by conducting a sine sweep test, the average of the 24 for the SBMs and the average of the 2 for the thrust AMB are fitted with different transfer functions, because the power supply of the thrust amplifiers, the resistance and inductance of the thrust coils are significantly different from those of SBMs, but of the same form:

$$G_{amp} = \frac{b_1 s + b_0}{s^2 + a_1 s + a_0} \tag{5}$$

They are on the diagonal of the amp/coil transfer function matrix $[G_a(s)]$ in Fig. 3, relating the control voltage vector $\mathbf{V_c}$ to the current vector $\mathbf{i_c}$.

CONTROLLER DESIGN

The system is open loop unstable due to the negative stiffness present in both SBM and thrust AMB actuators, active control is indispensable for the shaft to be able to track and point. A set of 6 decoupled PID controllers is desired for all the 6 DOF, the models discussed above are used to design these controllers.

Figures 6 and 7 show the feedback control system for the two identical SBMs and the thrust AMB, respectively. The encoder and gap sensor signals are fed back into the digital signal processor (DSP) and decoded into the measurements for the shaft angular displacement θ, the radial displacements at the top SBM x_t and y_t, the radial displacements at the bottom SBM x_b and y_b, and the axial displacement z. The error signals between these measurements and the corresponding references are input into the 6 decoupled PID controllers. Because of the transconductance type amplifiers, the amplitudes of the amplifier voltages are calculated from the control voltages based on the same relation for the currents, as shown in Figs. 4 and 5. For each SBM, each segment voltage is then sinusoidally commutated into the three phase windings using digital commutation and three single-phase amplifiers. The three phase currents in each segment are 60° apart in phase angle and γ is the phase angle of the current with respect to the PM flux. Notice that the two SBMs share the same control loop in θ direction.

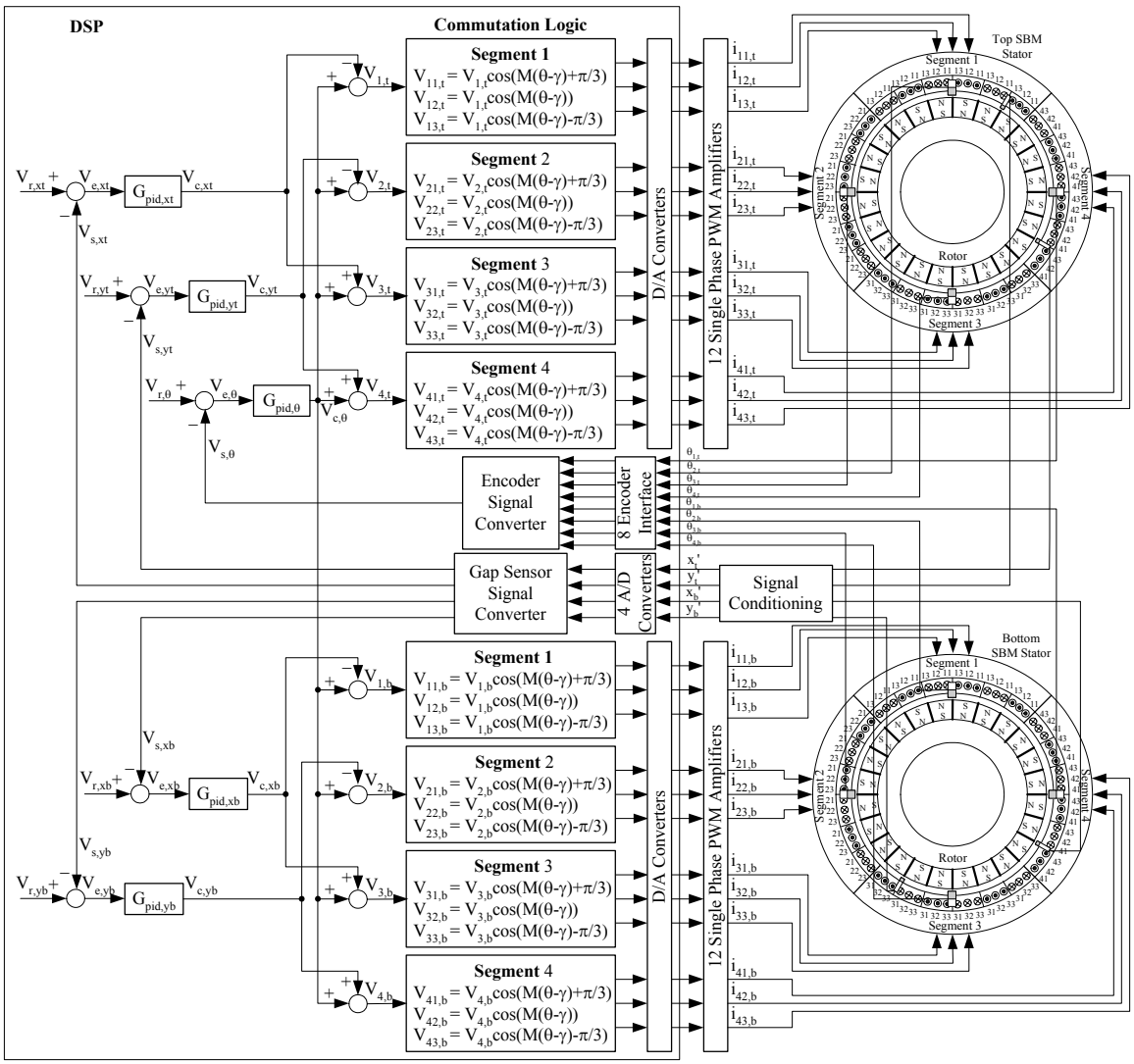

Figure 6. Control system for the top and bottom SBMs

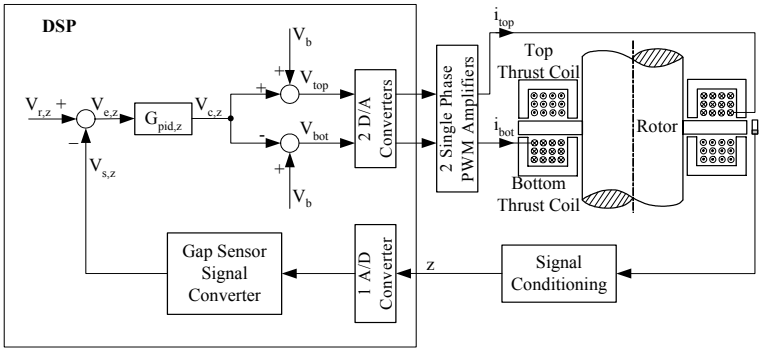

Figure 7. Control system for the thrust AMB

The control system is implemented on a dSPACE DS1005 DSP. The throughput rate of this DSP is much bigger than the system bandwidth limited by the amp/coil subsystem, a continuous model is used for the controllers. Each PID controller on the diagonal of the controller matrix $[G_c(s)]$ in Fig. 3 is then of the form:

$$G_{pid}(s) = K_P + \frac{K_I}{s} + K_D s \qquad (6)$$

The system is asymptotically stable in θ direction, and the four radial direction controllers are essentially the same, only two sets of stabilizing gains (one for radial and one for thrust direction) actually need to be found. The stable regions for these gains are searched to make the analytical system model stable. The gains picked out from these regions are then tried out and fine tuned experimentally on the test rig. The gains in θ direction are adjusted based on the speed and overshoot specifications in the time response. Finally, the shaft is successfully levitated in all six DOF and presents very good tracking and pointing performance, as shown by the experimental results in the next section.

EXPERIMENTAL RESULTS

Six PID controllers are implemented on the test rig so that the shaft is levitated in all 6 DOF. Figure 8 shows the tracking performance of the system to a sinusoidal reference input of 1 Hz frequency and 7.2º amplitude in angular direction. Both the desired and actual traces are shown, the angular slewing is clearly quite smooth and accurate.

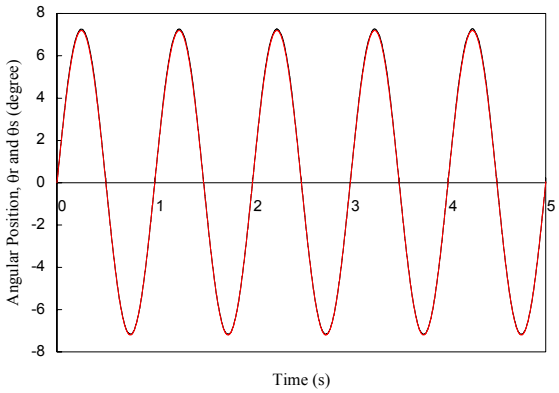

Figure 8. Angular slewing at frequency=1Hz and amplitude=7.2˚

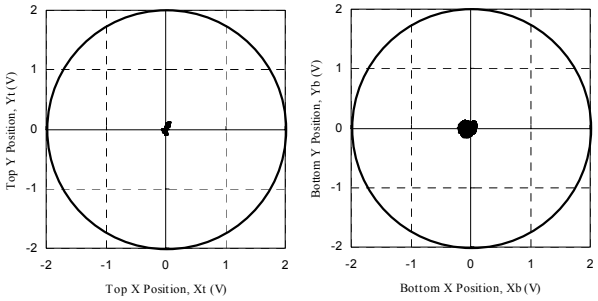

Figure 9. Radial orbits at the upper and lower ends of the shaft during the large angle slewing

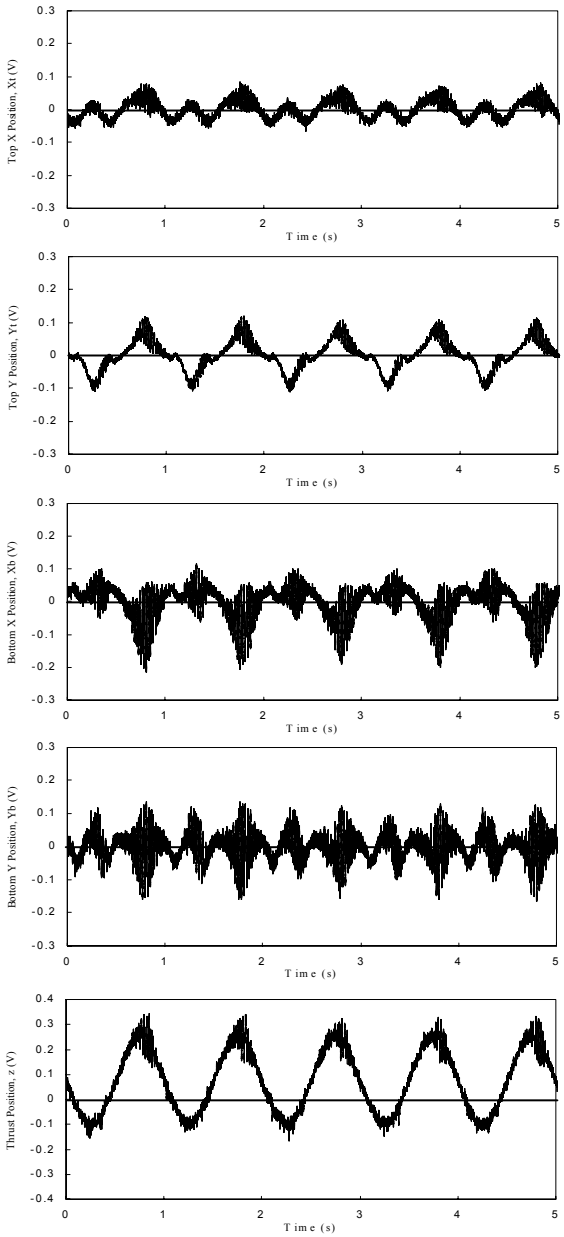

Figure 10. Lateral displacements during the large angle slewing

Figure 9 depicts the radial orbits at the upper and lower ends of the shaft during the large angle slewing, and Fig. 10 details the traces of the shaft motions in the 5 lateral DOF, including the radial at both ends and the axial positions. The output signals of the five probes have all been scaled to ±2V inside the DSP, with 0V representing the centered position in the clearance air gap. It's seen that the stable levitation is well maintained throughout the tracking. The lower end has slightly bigger radial displacements than the upper end because the completely levitated shaft is not always straight inside the clearance air gap, the small variations

around the centered positions during the tracking are due to the low stiffness provided by the SBMs and the thrust AMB, given the controller gains currently used are not necessarily the optimal. The shaft is pulled up a little higher axially by increasing the reference in thrust direction to overcome the shaft weight of 70lbs.

To determine the pointing accuracy of the actuator, a series of 0.01Hz sine wave with decreasing amplitudes are used as the reference input, the shaft angular position from the eight high-resolution encoders is filtered by a 6th order low-pass butter-worth filter with a cut-off frequency of 5 rad/s and captured together with the sinusoidal reference. The filter helps to distinguish the actual system response to the small input from the higher frequency electrical noise present in the system. Figure 11 shows the system response to a sine wave with peak amplitude of 6.28 μrad. The shaft clearly follows the reference and the jerkiness is due to the system noise lower than 5 rad/s. By further reducing the input signal level, the pointing accuracy of the system is determined to be 377nrad or better.

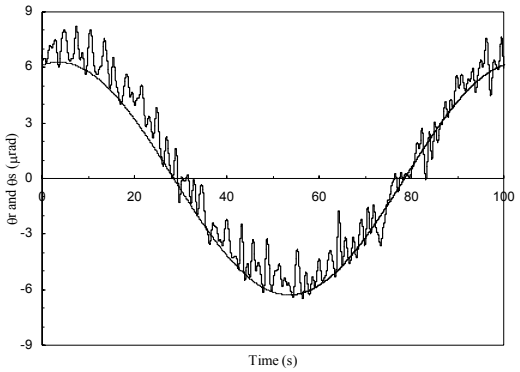

Figure 11. System response to a sine wave with peak amplitude 6.28μrad and frequency 0.01Hz

CONCLUSIONS

This paper presents a linear system model for a six DOF electromagnetic gimbal prototype system. A set of six decoupled PID controllers is designed based on this model and used to successfully levitate the test rig in all the six directions experimentally. The actuator demonstrates a very good tracking and pointing performance in θ direction and good stabilization in all the other directions. The pointing accuracy of 377nrad confirms the great potential of the slotless SBM as an excellent candidate in precision pointing applications.

ACKNOWLEDGMENTS

The authors express their appreciation to Airex Corporation of Dover, NH, USA, for partial sponsorship of this research.

REFERENCES

[1] Carroll, D., Sedgewick, J., and Stephens, L.S., 1999, "Long life, fault tolerant, spacecraft sensor gimbal/bearing system final report," United States Air Force Research Laboratory/VSDV, Contract No. F29601-98-C-0188.

[2] Stephens, L.S., and Kim, D.G., 2001, "Analysis and simulation of a Lorentz-type, slotless sellf-bearing motor," IFAC Journal of Control Engineering Practice, July, pp.899-905.

[3] Stephens, L.S., and Kim, D.G., 2002, "Force and torque characteristics for a slotless, Lorentz self bearing servomotor," IEEE Transactions on Magnetics, 38, pp.1764-1773.

[4] Kim, D.G. and Stephens, L.S., 2000, "Fault tolerance of a Lorentz-type self bearing motor according to the coiling schemes," *Proc. 7th Int. Symp. Magn. Bearings*, ETH, Zurich, Switzerland, pp.219-224.

[5] Steele, B.A. and Stephens, L.S., 2000, "A test rig for measuring force and torque production in a Lorentz, slotless self bearing motor," *Proc. 7th Int. Symp. Magn. Bearings*, ETH, Zurich, Switzerland, pp.407-412.

[6] Chiba, A., Rahman, M.A., and Fukao, T., 1991, "Radial forces in bearingless reluctance motor," IEEE Transactions on Magnetics, 27, p. 786.

[7] Okada, Y., Konishi, H., Kanebako, H., and Lee, C.W., 2000, "Lorentz force type self bearing motor," *Proc. 7th Int. Symp. Magn. Bearings*, Zurich, pp.353-358.

[8] Stephens, L.S., 2001, "Dynamic modeling and validation of a Lorentz self bearing motor test rig," *Proceedings of the ASME IGTI 2001 Conference*, ASME Paper No. 2001-GT-0567.

[9] Stephens, L.S., and Chin, H.M., 2003, "Robust stability of the Lorentz-type self bearing servomotor," JSME International Journal, Series C, 46, pp. 355-362.

[10] Chin, H.M., and Stephens, L.S., 2003, "Closed loop performance of a slotless Lorentz self-bearing motor," *Proceedings of the ASME IGTI 2003 Conference*, ASME Paper No. GT-2003-38750.